Crystal structures and magnetic properties of verdazyl-based complexes with transition metals

H. Tsukiyama,[1] S. Morota,[1] S. Shimono,[2] Y. Iwasaki,[3] M. Hagiwara,[4] Y. Hosokoshi,[1] and H. Yamaguchi[1,*]

[1]*Department of Physical Science, Osaka Metropolitan University, Osaka 599-8531, Japan*

[2]*Department of Materials Science and Engineering, National Defense Academy, Kanagawa 239-8686, Japan*

[3]*Department of Physics, College of Humanities and Sciences, Nihon University, Tokyo 156-8550, Japan*

[4]*Center for Advanced High Magnetic Field Science (AHMF), Graduate School of Science, Osaka University, Osaka 560-0043, Japan*

(Received 24 July 2022; revised 28 August 2022; accepted 16 September 2022; published 30 September 2022)

Verdazyl-based complexes, $[Zn(hfac)_2](m\text{-Py-V})_2 \cdot CH_3CN$ and $[Cu(hfac)_2][m\text{-Py-V-}(p\text{-F})_2]_2$, were successfully synthesized. For $[Zn(hfac)_2](m\text{-Py-V})_2 \cdot CH_3CN$, molecular orbital (MO) calculations indicated the formation of a spin-$\frac{1}{2}$ antiferromagnetic (AFM) chain with fourfold magnetic periodicity consisting of three types of exchange interactions. We quantitatively explained the magnetic properties based on the expected spin model. For $[Cu(hfac)_2][m\text{-Py-V-}(p\text{-F})_2]_2$, MO calculations indicated the formation of a spin-$\frac{1}{2}$ spin lattice, topologically equivalent to distorted octagons arranged two-dimensionally. We reproduced the observed magnetic properties assuming a spin-$\frac{1}{2}$ AFM dimer of radical spins, with residual Cu spins exhibiting paramagnetic behavior. Furthermore, we evaluated the anisotropic g values from the electron spin resonance absorption spectra, confirming that the low-temperature magnetic properties are mainly attributed to the Cu spins. These results demonstrate the realization of unconventional spin systems composed of organic radicals and transition metals and propose an effective method for spin arrangement design.

DOI: 10.1103/PhysRevMaterials.6.094417

I. INTRODUCTION

Organic radicals have spin-$\frac{1}{2}$ in one molecule and form various spin models as building blocks through intermolecular magnetic interactions. Complexes that combine metals and organic radicals (metal-radical complexes) are expected to further expand the possibilities of organic system-based material design. Precise control of the magnetic interaction between a metal and radical is crucial for the design of molecule-based functions. The coordination geometry around the metal center determines the absolute value and sign of the metal-radical exchange coupling. Numerous metal-radical complexes have been reported thus far by using radical ligands, such as nitroxide, benzosemiquinonoid, and thiazyl, which exhibit interesting magnetic properties [1]. Direct orbital overlaps between metals and radicals cause strong exchange couplings and form metal-radical hybrid spins in low-temperature regions [2–4]. Furthermore, the use of radicals that bridge two or more transition metals provides remarkable materials such as molecule-based magnets [5] and mixed-spin chains [6]. The verdazyl radical, which is the focus of this paper, can also be a stable ligand and has been intensively investigated thus far [7–11].

Our material design using verdazyl radicals with diverse molecular structures has demonstrated the realization of unconventional spin-$\frac{1}{2}$ systems [12–17]. Recently, we have developed the synthesis method of metal-radical complexes using a combination of 3*d* transition metals and verdazyl radicals [18–24]. We synthesized verdazyl-based complexes $[M(hfac)_2](o\text{-Py-V})$ [18,19] and $[M(hfac)_2][o\text{-Py-V-(4-F)}_2]$ (M = Zn, Mn) [22,23], where hfac is 1,1,1,5,5,5-hexafluoro-2,4-pentanedione, *o*-Py-V is 3-(2-pyridinyl)-1,5-diphenylverdazyl, and *o*-Py-V-(4-F)$_2$ is 3-(2-pyridinyl)-1,5-bis(4-fluorophenyl)verdazyl. The Zn-verdazyl complexes $[Zn(hfac)_2](o\text{-Py-V})$ and $[Zn(hfac)_2][o\text{-Py-V-(4-F)}_2]$ formed a spin-$\frac{1}{2}$ alternating chain and honeycomb lattice, respectively. The crystal structures of the Mn-verdazyl complexes are isomorphous with those of the Zn-verdazyl complexes. Furthermore, the exchange coupling J_{intra} between spins on Mn^{2+} ($S_{Mn} = \frac{5}{2}$) and verdazyl radicals ($S_V = \frac{1}{2}$), defined by the spin Hamiltonian $H = J_{intra} S_{Mn} \cdot S_V$, was evaluated to be $\sim$330 K for both complexes, forming an $S = 2$ hybrid spin $<\sim$100 K. Accordingly, the low-temperature magnetic properties of Mn-verdazyl complexes are adequately explained by spin-2 systems with small onsite biaxial anisotropy derived from transition metals. These results demonstrate that our material design using radical-based complexes can convert spin-$\frac{1}{2}$ systems to spin-2 systems through metal-radical couplings.

The verdazyl-based complexes we have synthesized thus far have direct coordination between the radical center and the transition metal, yielding strong antiferromagnetic (AFM) metal-radical exchange couplings. In such cases, however, spins on the radicals form a nonmagnetic singlet state with a spin-$\frac{1}{2}$ particle on the metal, and thus, the absolute value of the exchange couplings between radical spins is suppressed <1 K [19,23]. As the next step in our material design, we aimed to form mixed-spin systems by effectively combining intramolecular and intermolecular interactions in verdazyl-based complexes. It is expected that their nondirect coordination with the radical

*h_yamaguchi@omu.ac.jp

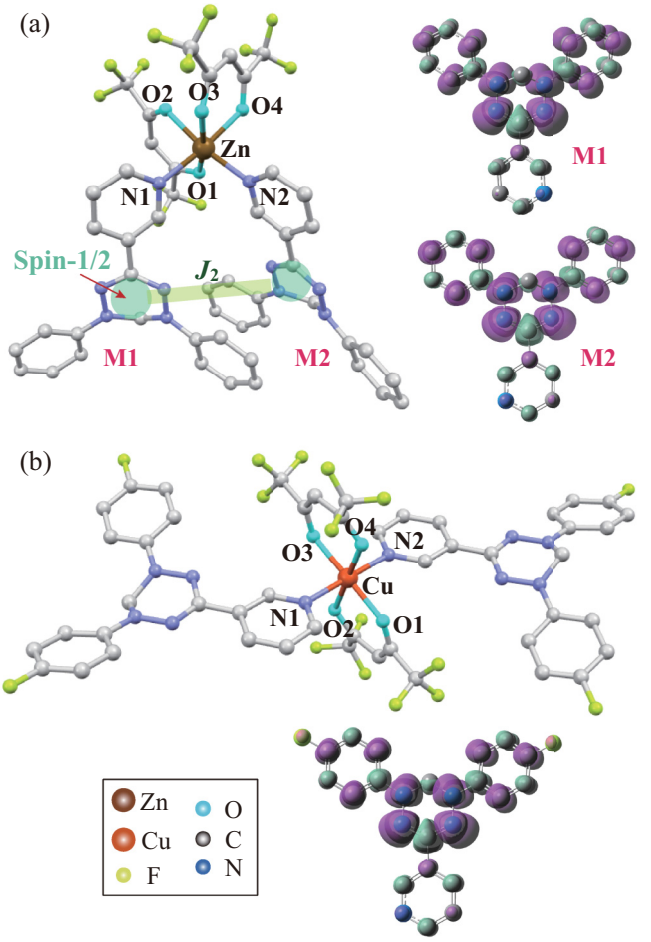

FIG. 1. Molecular structure and spin-density distribution on radicals of (a) $[Zn(hfac)_2](m\text{-Py-V})_2 \cdot CH_3CN$ and (b) $[Cu(hfac)_2][m\text{-Py-V-}(p\text{-F})_2]_2$. Hydrogen atoms are omitted for clarity. The purple and light green shapes correspond to positive and negative spin densities, respectively. The isodensity surface corresponds to a cutoff value of $0.001e$ Bohr^{-3}. The circles at the center of *m*-Py-V represent spin $\frac{1}{2}$ on the radical. The thick line shows intramolecular exchange interaction J_2 originating from the overlapping of the π orbitals on *m*-Py-V.

center can make the energy scales of the metal-radical and radical-radical exchange couplings comparable. We recently established techniques for synthesizing verdazyl-based complexes with nondirect coordination to the radical center.

In this paper, we present verdazyl-based complexes without direct coordination with the radical center. We successfully synthesized single crystals of $[Zn(hfac)_2](m\text{-Py-V})_2 \cdot CH_3CN$ [*m*-Py-V = 3-(3-pyridinyl)-1,5-diphenylverdazyl] [Fig. 1(a)] and $[Cu(hfac)_2][m\text{-Py-V-}(p\text{-F})_2]_2$ [*m*-Py-V-$(p$-F$)_2$ = 3-(3-pyridinyl)-1,5-bis(4-fluorophenyl)verdazyl] [Fig. 1(b)]. These complexes demonstrated the formation of spin-$\frac{1}{2}$ quantum spin models composed of intramolecular and intermolecular exchange interactions. For $[Zn(hfac)_2](m\text{-Py-V})_2 \cdot CH_3CN$, the *m*-Py-V radical has a spin-$\frac{1}{2}$, and the molecular orbital (MO) calculation indicated the formation of a spin-$\frac{1}{2}$ AFM chain with fourfold magnetic periodicity. We quantitatively explained the magnetic properties based on the expected spin model. For $[Cu(hfac)_2][m\text{-Py-V-}(p\text{-F})_2]_2$, the *m*-Py-V-$(p$-F$)_2$ radical and the Cu^{2+} ion have a spin $\frac{1}{2}$, and the MO calculation indicated the formation of a spin-$\frac{1}{2}$ spin lattice topologically equivalent to distorted octagons arranged two-dimensionally. The magnetic properties indicated the formation of a singlet dimer of radical spins coupled by the strong AFM interaction. The paramagnetic behavior observed in the low-temperature region is considered to originate from the residual Cu spins. We quantitatively explained the magnetic properties based on the spin-$\frac{1}{2}$ AFM dimer of radical spins, with residual Cu spins exhibiting paramagnetic behavior. Furthermore, we evaluated the anisotropic *g* values from the electron spin resonance (ESR) absorption spectra, confirming that the low-temperature magnetic properties mainly originate from the Cu spins.

II. EXPERIMENTAL

We synthesized *m*-Py-V and *m*-Py-V-$(p$-F$)_2$ through a conventional procedure for a verdazyl radical [25]. For $[Zn(hfac)_2](m\text{-Py-V})_2$, a solution of $Zn(hfac)_2{\cdot}2H_2O$ (309 mg, 0.6 mmol) in 15 mL of heptane was refluxed at 60 °C. A solution of *m*-Py-V (189 mg, 0.6 mmol) in 2 mL of CH_2Cl_2 was slowly added, and stirring was continued for 1 h. After the mixed solution cooled to room temperature, a dark-green crystalline solid of $[Zn(hfac)_2](m\text{-Py-V})_2 \cdot CH_3CN$ was separated by filtration and washed with heptane. The dark-green residue was recrystallized using acetonitrile at 10 °C. For $[Cu(hfac)_2][m\text{-Py-V-}(p\text{-F})_2]_2$, a solution of $Cu(hfac)_2{\cdot}2H_2O$ (154 mg, 0.3 mmol) in 15 mL of heptane was refluxed at 60 °C. A solution of *m*-Py-V-$(p$-F$)_2$ (105 mg, 0.3 mmol) in 2 mL of CH_2Cl_2 was slowly added, and stirring was continued for 1 h. After the mixed solution cooled to room temperature, brownish-green crystalline solid of $[Cu(hfac)_2][m\text{-Py-V-}(p\text{-F})_2]_2$ was separated by filtration and washed with heptane. The brownish-green residue was recrystallized using ethanol at 10 °C.

The crystal structure was determined from the intensity data obtained using a Bruker D8 VENTURE with a PHOTON II detector. The structure was determined via a direct method using SIR2004 [26] and was refined using the SHELXL97 crystal structure refinement program [27]. The structural refinement was carried out using anisotropic and isotropic thermal parameters for the nonhydrogen and hydrogen atoms, respectively. All the hydrogen atoms were placed at the calculated ideal positions. The magnetization was measured using a commercial superconducting quantum interference device magnetometer (MPMS-XL, Quantum Design). The experiments were performed using randomly oriented small single crystals. The experimental results were corrected for the diamagnetic contribution, which are determined based on the numerical analysis to be described and confirmed to be close to those calculated by Pascal's method. The ESR measurements were performed using a vector network analyzer (ABmm), superconducting magnet (Oxford Instruments), and a laboratory-built cylindrical cavity. We used small crystals with typical dimensions $<10^{-3}$ mm^3 as powder samples for the ESR measurements.

Ab initio MO calculations were performed using the UB3LYP method as broken-symmetry hybrid density

TABLE I. Crystallographic data for $[Zn(hfac)_2](m\text{-Py-V})_2 \cdot CH_3CN$ (**A**) and $[Cu(hfac)_2][m\text{-Py-V-}(p\text{-F})_2]_2$ (**B**).

Sample	**A**	**B**
Formula	$C_{50}H_{37}F_{12}N_{11}O_4Zn$	$C_{48}H_{30}F_{16}N_{10}O_4Cu$
Crystal system	Triclinic	
Space group	$P\bar{1}$	
Temperature	Room temperature	
a/Å	10.5527(9)	10.8445(4)
b/Å	15.4753(13)	11.0606(4)
c/Å	16.5716(14)	12.1628(5)
α/deg.	75.475(3)	73.6510(10)
β/deg.	86.258(3)	83.3050(10)
γ/deg.	79.576(3)	61.6790(10)
V/Å^3	2576.0(4)	1232.09(8)
Z	2	1
D_{calc}/g cm^{-3}	1.482	1.588
Total reflections	8481	4028
Reflection used	5169	3470
Parameters refined	704	359
$R\ [I > 2\sigma(I)]$	0.0773	0.0477
$R_w\ [I > 2\sigma(I)]$	0.1755	0.1193
Goodness of fit	1.008	1.043
The Cambridge Crystallographic Data Centre	2192253	2192254

TABLE II. Bond distances (Å) and angles (deg.) related to the transition metals for $[Zn(hfac)_2](m\text{-Py-V})_2 \cdot CH_3CN$ (**A**) and $[Cu(hfac)_2][m\text{-Py-V-}(p\text{-F})_2]_2$ (**B**).

A		**B**	
Zn–N1	2.12	Cu–N1	2.05
Zn–N2	2.11	Cu–N2	2.05
Zn–O1	2.10	Cu–O1	2.02
Zn–O2	2.15	Cu–O2	2.28
Zn–O3	2.07	Cu–O3	2.02
Zn–O4	2.15	Cu–O4	2.28
N1–Zn–N2	98.3	O1–Cu–N1	89.2
N2–Zn–O4	87.7	N1–Cu–O3	90.8
O4–Zn–O2	82.7	O3–Cu–N2	89.2
O2–Zn–N1	91.3	N2–Cu–O1	90.8
N1–Zn–O1	88.1	N1–Cu–O4	84.8
O1–Zn–O4	91.8	O4–Cu–N2	95.2
O4–Zn–O3	85.6	N2–Cu–O2	84.8
O3–Zn–N1	93.4	O2–Cu–N1	95.2
N2–Zn–O3	97.0	O1–Cu–O2	86.5
O3–Zn–O2	84.0	O2–Cu–O3	93.5
O2–Zn–O1	84.5	O3–Cu–O4	86.5
O1–Zn–N2	94.0	O4–Cu–O1	93.5

functional theory calculations. All calculations were performed using the GAUSSIAN09 software package. The basis sets are 6-31G (intermolecule) and 6-31G(d, p) (intramolecule). The convergence criterion was set to 10^{-8} Hartree. To estimate the intermolecular exchange interaction of the molecular pairs, we employed a conventional evaluation scheme [28].

The quantum Monte Carlo (QMC) code is based on the directed loop algorithm in the stochastic series expansion representation [29]. The calculations were performed for $N = 256$ under the periodic boundary condition, where N denotes the system size. It was confirmed that there is no significant size-dependent effect. All calculations were carried out using the ALPS application [30,31].

III. CRYSTAL STRUCTURE AND MAGNETIC MODEL

A. $[Zn(hfac)_2](m\text{-Py-V})_2 \cdot CH_3CN$

The crystallographic parameters of $[Zn(hfac)_2](m\text{-Py-V})_2 \cdot CH_3CN$ are summarized in Table I. Each m-Py-V radical has spin $\frac{1}{2}$. The nonmagnetic Zn atom is coordinated by two m-Py-V radicals, yielding an octahedral coordination environment. The bond lengths and angles of the Zn atom are listed in Table II. The results of the MO calculations on m-Py-V indicated that ∼63% of the total spin density is present on the central verdazyl ring (which includes four N atoms), and each phenyl ring accounts for ∼13–18% of the relatively large total spin density, as shown in Fig. 1(a). The pyridine rings coordinating to the Zn atom account for ∼6–7% of the total spin density. We evaluated the dominant exchange interactions by MO calculations and found three types of AFM interactions J_1, J_2, and J_3. They are evaluated as $J_1/k_B = 12$ K, $J_2/k_B = 4$ K, and $J_3/k_B = 38$ K; these are defined in the Heisenberg spin Hamiltonian given by $\mathcal{H} = J_n \sum_{\langle i,j \rangle} \mathbf{S}_i \cdot \mathbf{S}_j$, where $\sum_{\langle i,j \rangle}$ denotes the sum over neighboring spin pairs. The m-Py-V pairs associated with these interactions have N-N and N-C short contacts and form a one-dimensional (1D) structure along the c axis, as shown in Fig. 2(a) Accordingly, the three evaluated interactions form a spin-$\frac{1}{2}$ chain along the c axis, as shown in Fig. 2(b). This spin chain is equivalent to a spin-$\frac{1}{2}$ J_1-J_2-J_3-J_2 AFM chain with fourfold periodicity in β-2,6-Cl_2-V [14]. In terms of molecular alignment, J_1 and J_3 are intermolecular interactions attributed to the overlapping of the π orbitals, and each m-Py-V pair is related by inversion symmetry. Here, J_2 is an intramolecular interaction, as shown in Fig. 1(a). The MO calculations demonstrated that the value of J_2 is almost independent of the coordination with Zn, indicating that it mainly originates from the overlapping of the π orbitals on m-Py-V. It is considered that the small spin densities on the coordinating pyridine rings suppress contribution of magnetic coupling via the Zn atom. Figure 2(c) shows the crystal structure viewed from the c axis, where the 1D chains run perpendicular to the plane. As the nonmagnetic hfac and CH_3CN are located between the 1D structures, the one-dimensionality of the present model is enhanced.

B. $[Cu(hfac)_2][m\text{-Py-V-}(p\text{-F})_2]_2$

The crystallographic parameters of $[Cu(hfac)_2][m\text{-Py-V-}(p\text{-F})_2]_2$ are summarized in Table I. As an inversion center exists at the Cu position, the two m-Py-V-$(p$-F$)_2$ radicals in the molecule are crystallographically equivalent, as shown in Fig. 1(b). Here, m-Py-V-$(p$-F$)_2$ and Cu^{2+} have spin $\frac{1}{2}$. The Cu atom is coordinated by two m-Py-V-$(p$-F$)_2$ radicals, yielding an octahedral coordination environment. The bond lengths and angles of the Cu atom are listed in Table II. The Jahn-Teller axis of Cu^{2+} lies along the O2-O4 vector. The results of the MO calculations for m-Py-V-$(p$-F$)_2$ indicated that ∼63%

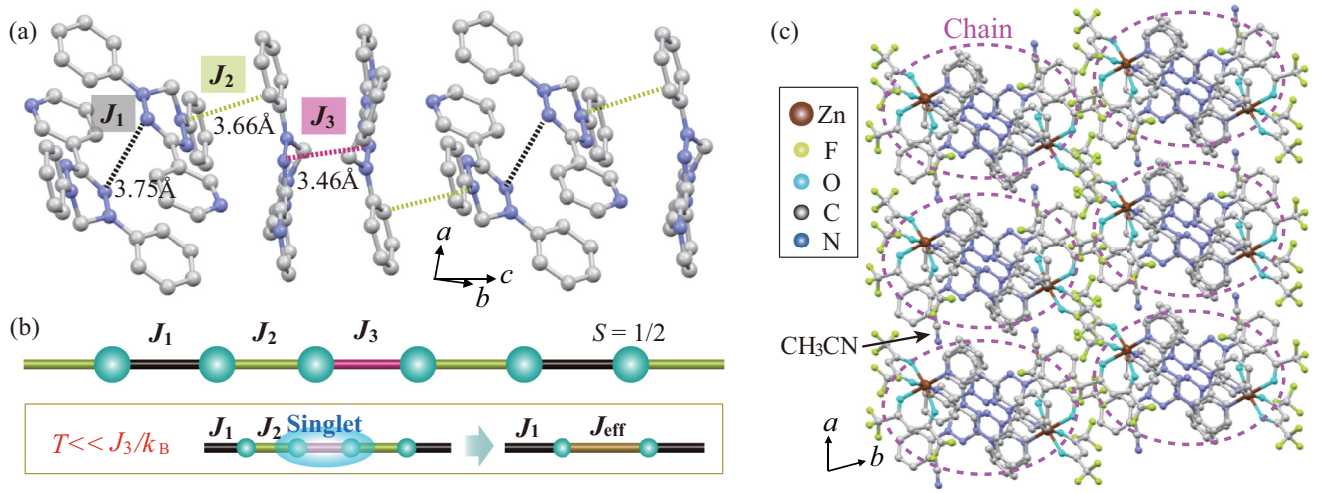

FIG. 2. (a) Crystal structure of $[Zn(hfac)_2](m\text{-Py-V})_2 \cdot CH_3CN$ forming a spin chain along the c axis. The dashed lines indicate the N-N and N-C short contacts associated with the exchange interactions. Hydrogen atoms, CH_3CN molecules, and $Zn(hfac)_2$ moieties are omitted for clarity. The radical pair associated with J_2 corresponds to the two radicals in the same molecule. (b) Corresponding spin-$\frac{1}{2}$ antiferromagnetic (AFM) chain with fourfold magnetic periodicity. For $T \ll J_3/k_B$, an effective spin-$\frac{1}{2}$ AFM alternating chain is formed by J_1 and J_{eff}. (c) Crystal structure viewed along the c axis. The broken line encloses the molecules comprising each spin chain structure.

of the total spin density is present on the central verdazyl ring, and each phenyl ring accounts for ∼15% of the relatively large total spin density, as shown in Fig. 1(b). The pyridine rings coordinating to the Cu atom account for ∼7% of the total spin density. We evaluated the intramolecular and intermolecular interactions, which are defined with $\mathcal{H} = J_n \sum_{\langle i,j \rangle} \mathbf{S}_i \cdot \mathbf{S}_j$, by using MO calculation. Although both the spin values of Cu and the radical are $\frac{1}{2}$, we assigned different spin sites, S_{Cu} and S_V, considering the difference in the g values. The intramolecular interaction J_{Cu} between S_{Cu} and S_V was evaluated to be ferromagnetic with −18 K, yielding a coupling of S_V-S_{Cu}-S_V for each molecule. For the intermolecular case, we found two types of dominant interactions between radicals, as shown in Figs. 3(a) and 3(b), which were evaluated as $J_{V1}/k_B = 81$ K and $J_{V2}/k_B = -8$ K. The short contacts associated with J_{V1} are related to the radical center with the highest spin density, which causes strong AFM exchange coupling. The m-Py-V-(p-F)$_2$ pairs associated with J_{V1} and J_{V2} are related through their inversion center and form a 1D overlap of MOs along the a axis, as shown in Fig. 3(c). Furthermore, the 1D overlaps are connected through the intramolecular J_{Cu}, forming a two-dimensional (2D) spin lattice in the ac plane, as shown in Figs. 3(c) and 3(d). From a topological perspective, this spin lattice can be regarded as distorted octagons arranged 2D and is an unconventional spin model that can be realized using our metal-radical complex. Figure 3(e) shows the crystal structure in the bc plane, where the 2D spin lattices are perpendicular to the plane. As the nonmagnetic hfac moieties are located between the spin lattices, the two-dimensionality of the spin system is enhanced.

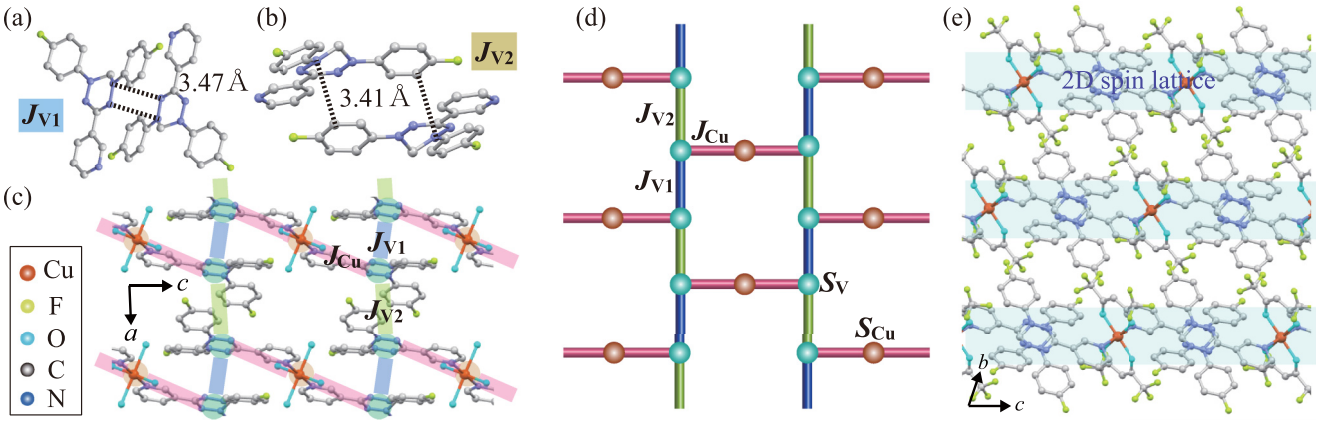

FIG. 3. Intermolecular radical pairs of $[Cu(hfac)_2][m\text{-Py-V-}(p\text{-F})_2]_2$ associated with exchange interactions (a) J_{V1} and (b) J_{V2}. Hydrogen atoms and hfac moieties are omitted for clarity. The dashed lines indicate N-N and N-C short contacts. (c) Crystal structure forming a two-dimensional (2D) spin lattice in the ac plane and (d) corresponding spin-$\frac{1}{2}$ spin model topologically equivalent to the distorted octagons arranged 2D. S_V and S_{Cu} represent the spins on the radical and Cu^{2+} ion, respectively. (e) Crystal structure in the bc plane. The thick lines represent the 2D spin planes.

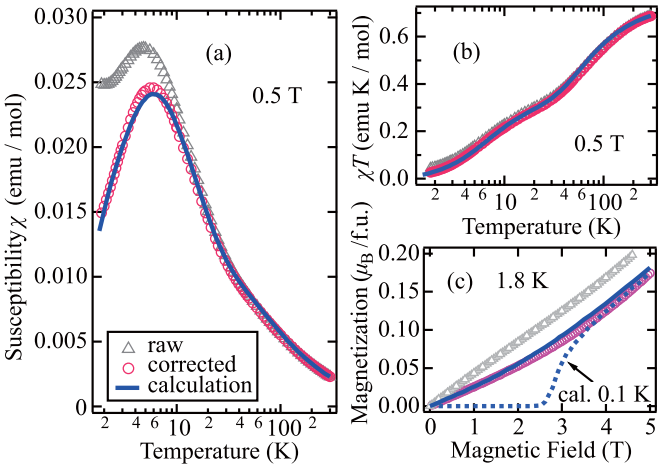

FIG. 4. Temperature dependence of (a) magnetic susceptibility ($\chi = M/H$) and (b) χT of [Zn(hfac)$_2$](m-Py-V)$_2$ · CH_3CN at 0.5 T. (c) Magnetization curve of [Zn(hfac)$_2$](m-Py-V)$_2$ · CH_3CN at 1.8 K. The open triangles denote raw data, and the open circles are corrected for the paramagnetic term due to the impurity. The solid lines represent the calculated results for the spin-$\frac{1}{2}$ antiferromagnetic (AFM) chain with fourfold periodicity. The broken line shows the calculated magnetization curve at 0.1 K, indicating an energy gap of 2.5 T.

IV. MAGNETIC AND THERMODYNAMIC PROPERTIES

A. [Zn(hfac)$_2$](m-Py-V)$_2$ · CH_3CN

Figure 4(a) shows the temperature dependence of the magnetic susceptibility ($\chi = M/H$) of [Zn(hfac)$_2$](m-Py-V)$_2$ · CH_3CN at 0.5 T, showing a broad peak at ∼5 K. The temperature dependence of χT shows a two-step decrease with decreasing temperature, as shown in Fig. 4(b). This behavior is expected to be associated with the formation of two types of singlet states in the spin-$\frac{1}{2}$ J_1-J_2-J_3-J_2 AFM chain [14]. Assuming the conventional paramagnetic behavior $C_{\rm imp}/T$, where $C_{\rm imp}$ is the Curie constant of the spin-$\frac{1}{2}$ impurities, we evaluated the paramagnetic impurities to be ∼2.6% of all spins, which is defined to fit the following calculated result and is close to those evaluated in other verdazyl radical crystals [12,18,32]. The corrected data in Fig. 4(a) correspond to χ obtained by subtracting the contribution of the impurities from the raw data and clearly exhibit a rapid decrease with decreasing temperature below the peak temperature, which is indicative of the formation of a singlet state with an excitation gap. Figure 4(c) shows the magnetization curve at 1.8 K. We subtracted the same amount of paramagnetic impurities as evaluated from the magnetic susceptibility assuming the Brillouin function. The corrected magnetization curve without paramagnetic contribution clearly exhibits nonlinear behavior attributed to strong quantum fluctuations, as shown in Fig. 4(c).

We calculated the magnetic susceptibility based on the spin chain using the QMC method. The spin Hamiltonian is expressed as

$$\mathcal{H} = \sum_j (J_1 \mathbf{S}_{4j-3}\cdot\mathbf{S}_{4j-2} + J_2 \mathbf{S}_{4j-2}\cdot\mathbf{S}_{4j-1} + J_3 \mathbf{S}_{4j-1}\cdot\mathbf{S}_{4j} + J_2 \mathbf{S}_{4j}\cdot\mathbf{S}_{4j+1}) - g\mu_{\rm B} H \sum_j \mathbf{S}_j, \quad (1)$$

where $\mathbf{S}$ is the spin operator, g the g factor, $g = 2.00$, $\mu_{\rm B}$ the Bohr magneton, and H the external magnetic field. We confirmed the consistency between the experimental and calculated results by considering the parameters $J_1/k_{\rm B} = 11$ K ($J_1/J_3 = 0.10$), $J_2/k_{\rm B} = 34$ K ($J_2/J_3 = 0.32$), and $J_3/k_{\rm B} = 107$ K, as shown in Figs. 4(a)– 4(c). Note that the observed gapped behavior and two-step decrease in χT can be reproduced relatively well even with slightly different combinations of parameters. The arbitrariness of the parameters in the analysis suggests that the actual values are within the following ranges: $J_1/J_3 = 0.05$–0.15 and $J_2/J_3 = 0.2$–0.4. Because the absolute values of J_2 and J_3 are relatively larger than those from MO evaluations, the overlap of π orbitals associated with these interactions should be enhanced owing to lattice shrinkage at low temperatures. It should be noted that the obtained parameters are close to those in β-2,6-Cl_2-V, where $J_1/J_3 = 0.11$ and $J_2/J_3 = 0.44$ [14]. Accordingly, the low-temperature effective state of the present spin model is like that in β-2,6-Cl_2-V. For $T \ll J_3/k_{\rm B}$, two spins connected by the strongest AFM J_3 become nonmagnetic with the formation of a singlet dimer. However, an effective interaction $J_{\rm eff}$ works between the remaining spins connected by J_1 through the triplet excited states of the singlet dimer, as shown in Fig. 2(b). From the second-order perturbation treatment of J_2 in the spin Hamiltonian, $J_{\rm eff}$ is given by $J_2^2/2J_3$ [14,33,34]. Consequently, the effective state in the low-temperature region can be regarded as a spin-$\frac{1}{2}$ AFM alternating chain composed of J_1 and $J_{\rm eff}$, where the stronger J_1 forms a singlet dimer with an excitation energy gap. The calculated magnetization curve at 0.1 K for the present model indeed exhibits the corresponding gapped behavior with an energy gap of 2.5 T, as shown in Fig. 4(c).

B. [Cu(hfac)$_2$][m-Py-V-(p-F)$_2$]$_2$

Figures 5(a) and 5(b) show the temperature dependence of the magnetic susceptibility ($\chi = M/H$) and χT of [Cu(hfac)$_2$][m-Py-V-(p-F)$_2$]$_2$ at 0.5 T, respectively. Here, χT exhibits a steep decrease with decreasing temperatures until ∼20 K, indicating the formation of a singlet dimer of $S_{\rm V}$ coupled by the strong AFM $J_{\rm V1}$. The paramagnetic behavior observed in the lower temperature region originates from the residual $S_{\rm Cu}$ spins. We calculated the magnetic susceptibility of the spin-$\frac{1}{2}$ AFM dimer with paramagnetic contribution, assuming the conventional paramagnetic behavior $C_{\rm Cu}/T$, where $C_{\rm Cu}$ is the Curie constant of $S_{\rm Cu}$. Consequently, we confirmed the consistency of the experimental results with the calculated results for $J_{\rm V1} = 124$ K and $C_{\rm Cu} = 0.476$, as shown in Figs. 5(a) and 5(b). The evaluated value of $C_{\rm Cu}$ indicates that the average g value of $S_{\rm Cu}$ is 2.25. The magnetization curves in the low-temperature regions are indeed explained by Brillouin function for free spin-$\frac{1}{2}$ with $g = 2.25$, as shown in Fig. 5(c). Slight deviations are found in the low-temperature regions, which is especially apparent for $\chi T <$∼10 K, as shown in the inset of Fig. 5(b). These deviations are attributed to the contribution of weak AFM interactions between $S_{\rm Cu}$ spins. We can roughly evaluate the energy scale of the weak additional interactions using a mean-field approximation. For magnetic susceptibility, the mean-field approximation gives $\chi = \chi_{\rm cal}/(1 + zJ'\chi_{\rm cal})$, where $\chi_{\rm cal}$ is the magnetic susceptibility

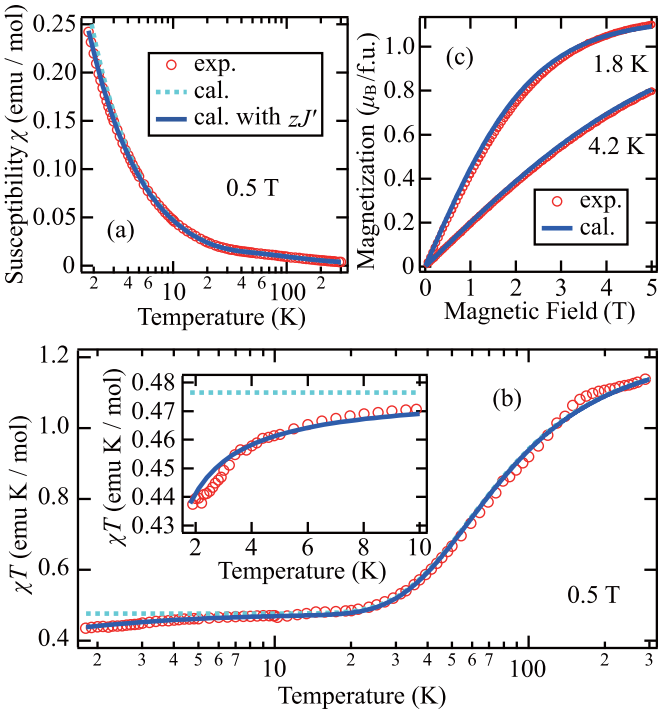

FIG. 5. Temperature dependence of (a) magnetic susceptibility ($\chi = M/H$) and (b) χT of $[Cu(hfac)_2][m\text{-Py-V-}(p\text{-F})_2]_2$ at 0.5 T. The solid and broken lines represent the calculated results for the spin-$\frac{1}{2}$ antiferromagnetic (AFM) dimer of S_V with paramagnetic contribution of S_{Cu} and those considering the effective interactions between S_{Cu} spins, respectively. The inset shows the expansion of the low-temperature region. (c) Magnetization curves at 1.8 and 4.2 K. The solid lines represent the Brillouin function for spin-$\frac{1}{2}$ with the averaged g value.

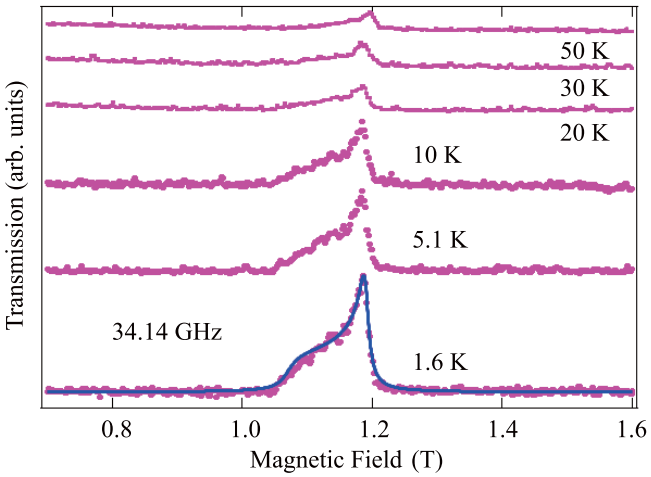

FIG. 6. Temperature dependence of electron paramagnetic resonance (ESR) absorption spectra of $[Cu(hfac)_2][m\text{-Py-V-}(p\text{-F})_2]_2$ at 34.14 GHz. The solid line represents the powder pattern simulation.

calculated assuming an S_V dimer and an S_{Cu} free spin, z is the number of nearest-neighbor S_{Cu} spins, and J' is the effective interaction between S_{Cu} spins. The consistency between the experimental and calculated results was verified using $zJ' = 0.64$ K, as shown in Fig. 5(b). Considering the spin model expected from the MO calculation, the effective interactions are expected to be caused through the triplet excited states of the S_V dimer coupled by J_{V1} by the same origin as in the case of the above Zn compound. From the second-order perturbation treatment of J_{V2} and J_{Cu} in the spin Hamiltonian, the most dominant effective interaction is derived to be $J_{Cu}^2/2J_{V1}$ [14,33,34], forming an effective spin-$\frac{1}{2}$ AFM chain of S_{Cu} spins. Additionally, from the relation of $J_{Cu}^2/2J_{V1} = zJ'/2$, the actual value of J_{Cu} is evaluated to be ~ -9 K.

Figure 6 shows the temperature dependence of ESR absorption spectra at 34.14 GHz. It should be noted that the resonance signals become prominent <10 K, which is consistent with the abrupt increase in the magnetization in the low-temperature region. As the magnetic contributions in the low-temperature region are attributed to S_{Cu} spins, the enhanced resonance signals <10 K are paramagnetic resonances of $S_{Cu} = \frac{1}{2}$. Given that the S_V spin has a g value of 2.00 owing to the isotropic nature of our radical systems [35–37], a sharp resonance signal is expected to appear at ~1.22 T for 34.14 GHz. The observed resonance signals show lower resonance fields and broadening reflecting anisotropic g values, which demonstrates that the absorption spectra originate from S_{Cu} spins. The resonance spectra were simulated by assuming a Lorentzian line shape. The ESR powder pattern is obtained by numerically integrating the line shape, as expressed in the following form:

$$I(H) = \int_0^{2\pi}\int_0^{\pi} \frac{A}{1+\left(\frac{H-H_{res}}{\frac{\Delta H}{2}}\right)^2}\sin\theta d\theta d\phi, \qquad (2)$$

where A is a constant, H_{res} is the resonance field, and ΔH is the linewidth (full width at half maximum). The angular dependencies of H_{res} and ΔH can be expressed using the diagonal components of the principal axes and are given by

$$H_{res} = \frac{h\nu}{\mu_B\sqrt{g_x^2\sin^2\theta\cos^2\phi + g_y^2\sin^2\theta\sin^2\phi + g_z^2\cos^2\theta}}, \qquad (3)$$

$$\Delta H = \sqrt{\Delta H_x^2\sin^2\theta\cos^2\phi + \Delta H_y^2\sin^2\theta\sin^2\phi + \Delta H_z^2\cos^2\theta}, \qquad (4)$$

where h is the Planck constant, and ν is the measurement frequency. As the observed line shape is indicative of axial symmetry, which is consistent with the octahedral coordination environment close to tetragonal distortion, we assumed the following relations: $g_{xy} = g_x = g_y$ and $\Delta H_{xy} = \Delta H_x = \Delta H_y$. We then reproduced the observed line shape using $g_{xy} = 2.05$, $g_z = 2.28$, $\Delta H_{xy} = 130$ Oe, and $\Delta H_{xy} = 280$ Oe, as shown in Fig. 6. The g values of the principal axes result in

an average g value slightly smaller than that obtained from the magnetization data. It is considered that the nonuniform orientation of the small single crystals in the magnetization measurements caused a difference from the powder samples in the ESR measurement.

V. POSSIBILITY OF SPIN ARRANGEMENT DESIGN

We describe a possible spin arrangement design based on the present complexes. A beneficial feature of $[Zn(hfac)_2](m\text{-Py-V})_2 \cdot CH_3CN$ is that two m-Py-V radicals in the molecule have overlapping of π orbitals, yielding the AFM intramolecular interaction, as shown in Fig. 1(a). Therefore, the substitution of the nonmagnetic Zn with other magnetic $3d$ transition metals can form a triangular magnetic unit comprising two metal-radical and one radical-radical interactions. The triangular unit forms frustration through competing interactions that cannot be simultaneously satisfied and potentially induces various exotic quantum phenomena [38]. The introduction of metal-radical interactions into the present 1D chain is expected to form a 1D array of triangular units, where unconventional quantum many-body phenomena should emerge owing to the synergistic effects of one-dimensionality and frustration.

The Cu atom in $[Cu(hfac)_2][m\text{-Py-V-}(p\text{-F})_2]_2$ can also be substituted with other $3d$ transition metals with different spin sizes. The difference in spin size is significant for quantum spin systems and causes topologically different ground states [39–42]. Furthermore, the substitution of F atoms in m-Py-V-$(p$-F$)_2$ with other halogen atoms can modulate the overlapping of the π orbitals forming the exchange interactions through the electrostatic repulsion related to the halogen atoms. Such modulations on the MOs lead to the tuning of intermolecular exchange interactions [16,43,44]. If the strongest J_{V1} forming the large spin gap is suppressed by the modulations, the quantum properties associated with the magnetic excitations unique to the unconventional octagon model might become observable in the experimental magnetic fields.

VI. SUMMARY

We successfully synthesized single crystals of the verdazyl-based complexes $[Zn(hfac)_2](m\text{-Py-V})_2 \cdot CH_3CN$ and $[Cu(hfac)_2][m\text{-Py-V-}(p\text{-F})_2]_2$. These complexes demonstrated the formation of spin-$\frac{1}{2}$ quantum spin models composed of intramolecular and intermolecular exchange interactions. For $[Zn(hfac)_2](m\text{-Py-V})_2 \cdot CH_3CN$, the MO calculations indicated the formation of a spin-$\frac{1}{2}$ AFM chain with fourfold magnetic periodicity composed of three types of exchange interactions. We successfully explained the magnetic properties based on the expected spin model using the QMC method. In the low-temperature regions, one of the three interactions and the effective interaction formed a spin-$\frac{1}{2}$ AFM alternating chain with a spin gap. For $[Cu(hfac)_2][m\text{-Py-V-}(p\text{-F})_2]_2$, the MO calculations indicated the formation of a spin-$\frac{1}{2}$ spin lattice, topologically equivalent to distorted octagons arranged 2D. We assigned two spin-$\frac{1}{2}$ sites, S_{Cu} for Cu^{2+} ions and S_V for radicals, considering the difference of the g values. The spin lattice is composed of intramolecular interaction between S_{Cu} and S_V and two types of intermolecular interactions between S_V spins. The magnetic properties indicated the formation of an AFM singlet dimer of S_V spins. The paramagnetic behavior observed in the low-temperature region is considered to originate from the residual S_{Cu} spins. Consequently, we successfully explained the magnetic properties based on the spin-$\frac{1}{2}$ AFM dimer with paramagnetic contributions. Furthermore, we evaluated the effective interactions between S_{Cu} spins from the magnetization analysis and anisotropic g values of S_{Cu} from the ESR powder pattern analysis. In this paper, we demonstrated the realization of unconventional spin systems composed of organic radicals and transition metals. The combination of radicals and transition metals is quite diverse, thereby proposing an effective method for spin arrangement design. These complexes are expected to trigger the expansion of the quantum many-body phenomenon search into mixed-spin systems and stimulate a wide range of research areas related to magnetism in condensed matter.

ACKNOWLEDGMENTS

This paper was partly supported by the Asahi Glass Foundation. A part of this work was performed at the Center for Advanced High Magnetic Field Science in Osaka University under the interuniversity cooperative research program of the joint-research program of ISSP, the University of Tokyo.

[1] S. Demir, I. Jeon, J. R. Long. T. D. Harris, Coord. Chem. Rev. **289–290**, 149 (2015).
[2] D.-Z. Gao, Y.-Q. Sun, D.-Z. Liao, Z-H. Jiang, and S.-P. Yan, Z. anorg. allg. Chem. **634**, 1950 (2008).
[3] A. Okazawa, Y. Nagaichi, T. Nogami, and T. Ishida, Inorg. Chem. **47**, 8859 (2008).
[4] A. Okazawa and T. Ishida, Inorg. Chem. **49**, 10144 (2010).
[5] J. M. Manriquez, G. T. Yee, R. S. McLean, A. J. Epstein, and J. S. Miller, Science **252**, 1415 (1991).
[6] A. Caneschi, D. Gatteschi, N. Lalioti, C. Sangregorio, R. Sessoli, G. Venturi, A. Vindigni, A. Rettori, M. G. Pini, and M. A. Novak, Angew. Chem. Int. Ed. **40**, 1760 (2001).
[7] B. D. Koivisto and R. G. Hicks, Coord. Chem. Rev. **249**, 2612 (2005).
[8] C. W. Johnston, S. D. J. McKinnon, B. O. Patrick, and R. G. Hicks, Dalton Trans. **42**, 16829 (2013).
[9] T. M. Barclay, R. G. Hicks, M. T. Lemaire, and L. K. Thompson, Inorg. Chem. **40**, 5581 (2001).
[10] S. D. J. McKinnon, B. O. Patrick, A. B. P. Lever, and R. G. Hicks, Inorg. Chem. **52**, 8053 (2013).
[11] D. J. R. Brook, V. Lynch, C. Conklin, and M. A. Fox, J. Am. Chem. Soc. **119**, 5155 (1997).
[12] H. Yamaguchi, K. Iwase, T. Ono, T. Shimokawa, H. Nakano, Y. Shimura, N. Kase, S. Kittaka, T. Sakakibara, T. Kawakami *et al.*, Phys. Rev. Lett. **110**, 157205 (2013).

[13] H. Yamaguchi, A. Toho, K. Iwase, T. Ono, T. Kawakami, T. Shimokawa, A. Matsuo, and Y. Hosokoshi, J. Phys. Soc. Jpn. **82**, 043713 (2013).
[14] H. Yamaguchi, T. Okubo, K. Iwase, T. Ono, Y. Kono, S. Kittaka, T. Sakakibara, A. Matsuo, K. Kindo, and Y. Hosokoshi, Phys. Rev. B **88**, 174410 (2013).
[15] H. Yamaguchi, H. Miyagai, M. Yoshida, M. Takigawa, K. Iwase, T. Ono, N. Kase, K. Araki, S. Kittaka, T. Sakakibara *et al.*, Phys. Rev. B **89**, 220402(R) (2014).
[16] H. Yamaguchi, H. Miyagai, T. Shimokawa, K. Iwase, T. Ono, Y. Kono, N. Kase, K. Araki, S. Kittaka, T. Sakakibara *et al.*, J. Phys. Soc. Jpn. **83**, 033707 (2014).
[17] H. Yamaguchi, T. Okubo, S. Kittaka, T. Sakakibara, K. Araki, K. Iwase, N. Amaya, T. Ono, and Y. Hosokoshi, Sci. Rep. **5**, 15327 (2015).
[18] H. Yamaguchi, Y. Shinpuku, T. Shimokawa, K. Iwase, T. Ono, Y. Kono, S. Kittaka, T. Sakakibara, and Y. Hosokoshi, Phys. Rev. B **91**, 085117 (2015).
[19] H. Yamaguchi, Y. Shinpuku, Y. Kono, S. Kittaka, T. Sakakibara, M. Hagiwara, T. Kawakami, K. Iwase, T. Ono, and Y. Hosokoshi, Phys. Rev. B **93**, 115145 (2016).
[20] H. Yamaguchi, M. Okada, Y. Kono, S. Kittaka, T. Sakakibara, T. Okabe, Y. Iwasaki, and Y. Hosokoshi, Sci. Rep. **7**, 16144 (2017).
[21] N. Uemoto, Y. Kono, S. Kittaka, T. Sakakibara, T. Yajima, Y. Iwasaki, S. Miyamoto, Y. Hosokoshi, and H. Yamaguchi, Phys. Rev. B **99**, 094418 (2019).
[22] Y. Kono, T. Okabe, N. Uemoto, Y. Iwasaki, Y. Hosokoshi, S. Kittaka, T. Sakakibara, and H. Yamaguchi, Phys. Rev. B **101**, 014437 (2020).
[23] Y. Iwasaki, T. Okabe, N. Uemoto, Y. Kono, Y. Hosokoshi, S. Nakamura, S. Kittaka, T. Sakakibara, M. Hagiwara, T. Kawakami *et al.*, Phys. Rev. B **101**, 174412 (2020).
[24] H. Yamaguchi, N. Uemoto, T. Okubo, Y. Kono, S. Kittaka, T. Sakakibara, T. Yajima, S. Shimono, Y. Iwasaki, and Y. Hosokoshi, Phys. Rev. B **104**, L060411 (2021).
[25] R. Kuhn, Angew. Chem. **76**, 691 (1964).
[26] M. C. Burla, R. Caliandro, M. Camalli, B. Carrozzini, G. L. Cascarano, L. De Caro, C. Giacovazzo, G. Polidori, and R. Spagna, J. Appl. Crystallogr. **38**, 381 (2005).
[27] G. M. Sheldrick, SHELXL97, *Program for Crystal Structure Determination* (University of Göttingen, Germany, 1997).
[28] M. Shoji, K. Koizumi, Y. Kitagawa, T. Kawakami, S. Yamanaka, M. Okumura, and K. Yamaguchi, Chem. Phys. Lett. **432**, 343 (2006).
[29] A. W. Sandvik, Phys. Rev. B **59**, R14157(R) (1999).
[30] A. F. Albuquerque, F. Alet, P. Corboz, P. Dayal, A. Feiguin, L. Gamper, E. Gull, S. Gurtler, A. Honecker, R. Igarashi *et al.*, J. Magn. Magn. Mater. **310**, 1187 (2007); see also http://alps.comp-phys.org and http://wistaria.comp-phys.org/alps-looper/.
[31] B. Bauer, L. D. Carr, H. G. Evertz, A. Feiguin, J. Freire, S. Fuchs, L. Gamper, J. Gukelberger, E. Gull, S. Guertler *et al.*, J. Stat. Mech. (2011) P05001.
[32] S. Miyamoto, Y. Iwasaki, N. Uemoto, Y. Hosokoshi, H. Fujiwara, S. Shimono, and H. Yamaguchi, Phys. Rev. Mater. **3**, 064410 (2019).
[33] T. Masuda, A. Zheludev, B. Grenier, S. Imai, K. Uchinokura, E. Ressouche, and S. Park, Phys. Rev. Lett. **93**, 077202 (2004).
[34] M. Hase, M. Matsuda, K. Kakurai, K. Ozawa, H. Kitazawa, N. Tsujii, A. Dönni, M. Kohno, and X. Hu, Phys. Rev. B **76**, 064431 (2007).
[35] H. Yamaguchi, S. Nagata, M. Tada, K. Iwase, T. Ono, S. Nishihara, Y. Hosokoshi, T. Shimokawa, H. Nakano, H. Nojiri *et al.*, Phys. Rev. B **87**, 125120 (2013).
[36] H. Yamaguchi, Y. Tamekuni, Y. Iwasaki, R. Otsuka, Y. Hosokoshi, T. Kida, and M. Hagiwara, Phys. Rev. B **95**, 235135 (2017).
[37] H. Yamaguchi, Y. Iwasaki, Y. Kono, T. Okubo, S. Miyamoto, Y. Hosokoshi, A. Matsuo, T. Sakakibara, T. Kida, and M. Hagiwara, Phys. Rev. B **103**, L220407 (2021).
[38] L. Balents, Nature (London) **464**, 199 (2010).
[39] F. D. M. Haldane, Phys. Rev. Lett. **50**, 1153 (1983).
[40] I. Affleck, T. Kennedy, E. H. Lieb, and H. Tasaki, Phys. Rev. Lett. **59**, 799 (1987).
[41] E. Lieb and D. Mattis, J. Math. Phys. **3**, 749 (1962).
[42] M. Oshikawa, M. Yamanaka, and I. Affleck, Phys. Rev. Lett. **78**, 1984 (1997).
[43] H. Yamaguchi, T. Okita, Y. Iwasaki, Y. Kono, N. Uemoto, Y. Hosokoshi, T. Kida, T. Kawakami, A. Matsuo, and M. Hagiwara, Sci. Rep. **10**, 9193 (2020).
[44] H. Yamaguchi, T. Okita, Y. Iwasaki, Y. Kono, Y. Hosokoshi, T. Kida, A. Matsuo, T. Kawakami, and M. Hagiwara, J. Phys. Soc. Jpn. **90**, 064707 (2021).